Journal of Catalysis **211,** 326–334 (2002)
doi:10.1006/jcat.2002.3730

# Ce–Zr–Ca Ternary Mixed Oxides: Structural Characteristics and Oxygen Handling Properties

M. Fernández-García,*,[1] A. Martínez-Arias,* A. Guerrero-Ruiz,† J. C. Conesa,* and J. Soria*

*Instituto de Catálisis, CSIC, Campus Cantoblanco, 28049-Madrid, Spain; and †Departamento Química Inórganica y Técnica, UNED, 28040-Madrid, Spain

Received January 25, 2002; revised June 14, 2002; accepted June 27, 2002

**The structural/morphological and oxygen handling properties of Ce–Zr–Ca ternary mixed oxides prepared by a microemulsion method with a Zr : Ce atomic ratio close to 1 and with a Ca atomic content of 10 and 33 at% have been analyzed by using X-ray diffraction, transmission electron microscopy, infrared and Raman spectroscopies, electron spin resonance, and mass spectrometry using labeled $C^{18}O_2$ as reactant probe. The ternary oxides synthesized are nanostructured, with an average crystalline particle size around 2 nm, and always display tetragonal t″ symmetry. Their homogeneity in terms of chemical composition is reasonably good, although it decreases with the Ca content of the specimen. Ca introduction in a ceria–zirconia oxidic network strongly modifies surface and bulk oxygen handling properties. Surface properties are mainly modified by the depletion of Ce centers from the outermost layer and their concomitant electronic modification. Bulk oxygen diffusion is strongly altered and its behavior as a function of the Ca content slightly decays for low Ca doping and displays a large enhancement for the sample with the highest Ca concentration.** 

*Key Words:* **Ce–Zr–Ca ternary oxides; nanosize materials; oxygen handling properties; oxygen diffusion.**

## INTRODUCTION

The properties of some mixed oxide ceramics and their solid solutions depend on a series of factors, among which three are of capital importance: the particle size, the structural characteristics, and the chemical nonstoichiometry (1, 2). As is well-known, the properties of oxidic solids with industrial interest can be modulated or modified by acting on these three key parameters.

The case of ceria-based mixed oxides has technological implications for the present and future improvements of three-way catalysts (3), as well as of oxygen permeation membranes and fuel cells (4). Use of zirconium in nanosize ceria-based materials allows the stabilization of tetragonal structures displaying improved oxygen-handling properties and thermal stability with respect to the fluorite-type, cubic polymorph of ceria (3, 5). The former property has been related to the distortion of the oxygen sublattice, which leads to an enhancement of the anionic mobility (6). On the other hand, cationic dopants with oxidation state lower than +IV are frequently incorporated into the ceria lattice, typically leading to formation of intrinsic oxygen vacancies in order to maintain electroneutrality. In this case, differences in oxygen-handling properties with respect to ceria are expected to depend primarily on the size of the dopant (i.e., anion–cation bonding force) as well as on the energy of the vacancy–electron and vacancy–dopant associations (affecting, respectively, the mobility of excess electrons and, when present, of ions). In this context, the presence of $Ca^{2+}$ was shown to maximize the oxygen storage capacity of ceria with an increment of 40% (7). However, a recent study was able to show that the presence of $Ca^{2+}$ may enhance oxygen mobility at the surface but it considerably diminishes it at the bulk in nanosize materials (8). Additionally, the energetics of surface oxygen vacancy creation is severely modified on such materials (8).

The effect of combining two different heteroatoms in the ceria structure has been scarcely investigated (7, 9–11). In particular, the presence of three cations, Ce, Zr, and Ca, in ceramic materials with tetragonal structure has been shown to yield reasonable ionic mobility (on the order of that observed for Ca-doped $ZrO_2$); a strong relationship between the number of intrinsic/extrinsic oxygen vacancies and ionic mobility was then detected (10). However, to the best of our knowledge, the interplay between these factors and their potential implications in the oxygen handling properties have not been analyzed in nanosize Ce–Zr–Ca materials. As already noted, the particle size may strongly influence the behavior of the mixed oxide systems.

In this work, we have synthesized nanosize Ce–Zr–Ca ternary mixed oxides with different quantities of Ca and a Ce : Zr atomic ratio of 1. The preparation method is based on coprecipitation using a reverse microemulsion which can allow a precise control of the particle size, yielding narrow nanosize distributions, as well as a rigorous control (at least much better than conventional coprecipitation

[1] To whom correspondence should be addressed. Fax: +34-91-5854760. E-mail: m.fernandez@icp.csic.es.



0021-9517/02 $35.00

methods) of the chemical composition at a molecular scale (8, 12). The study intends to give a picture of the effect of Ca addition on Ce–Zr material with an atomic ratio close to 1, which, as is well-known, displays excellent oxygen-handling properties (3, 6, 12). These materials have been structurally/morphologically characterized and their oxygen-handling properties (particularly those related to catalytic behavior) analyzed in connection with the above-mentioned properties.

## EXPERIMENTAL

Two specimens were prepared by an inverse microemulsion method (12) with initial Ce : Zr : Ca atomic ratios of 9 : 9 : 2 and 1 : 1 : 1 in the reacting mixtures. The corresponding Ce(III), Zr(IV), and Ca(II) nitrates (Aldrich), with a global concentration of 0.5 M, were introduced in a reverse microemulsion (water—8 g—in oil) using *n*-heptane (58 g) as the organic phase, Triton X-100 (19 g; Aldrich), as surfactant and hexanol (15 g) as cosurfactant. This suspension was mixed with another one (having similar characteristics in terms of the water/organic concentrations) containing as aqueous phase an alkali solution (TMAH; Aldrich). The resulting mixtures, with all cations coprecipitated, were stirred for 24 h, centrifuged, decanted, and rinsed with methanol. After drying the solid portion overnight at 353 K, the resulting powders were calcined at 773 K for 2 h. These materials will be hereafter referred to as CZCa992 and CZCa111 (in correlation with the corresponding atomic ratios). Chemical analysis (by ICP–AES) showed differences of Ce : Zr : Ca atomic content within 10% of the nominal values. The Ce–Ca, Zr–Ca, and Ce–Zr binary mixed oxide references (which will be denoted using a similar nomenclature, e.g., CCaxx, ZCaxx, and CZxx) were prepared by a similar procedure and some of them have been described elsewhere (CCa (8) and CZ (12)). BET specific areas and average pore size of these materials are summarized in Table 1.

Powder X-ray diffraction (XRD) patterns were recorded on a Siemens D-500 diffractometer using nickel-filtered Cu $K\alpha$ radiation and operating at 40 kV and 25 mA. Spectra were taken with a 0.025° step size and using a counting time of 1 s per point. Fitting of XRD spectra were done by using Pearson VII functions and the Winfit! Program (© S. Krumm; http//www.geol.un-erlangen.de).

**TABLE 1**

**Textural Properties of CZCa, CCa, ZCa, and CZ Materials**

| Sample | $S_{BET}$ ($m^2\ g^{-1}$) | Average pore diameter (nm) |
|---|---|---|
| CZCa992 | 128 | 4 |
| CCa91 | 125 | 9.5 |
| ZCa91 | 130 | 4 |
| CZCa111 | 22 | 6 |
| CCa11 | 81 | 11 |
| ZCa11 | 47 | 6 |
| CZ11 | 122 | 9 |

Transmission electron microscopy (TEM) and electron diffraction (ED) experiments were carried out using a JEOL 2000 FX system (0.31-nm point resolution) equipped with a LINK (AN 10000) probe for energy dispersive X-ray spectroscopy (EDS) analysis. Portions of samples were crushed in an agate mortar and suspended in cyclohexene. After ultrasonic dispersion, a droplet was deposited on a copper grid supporting a perforated carbon film. Micrographs and electron diffractograms and, when appropriate, dark-field images were recorded over selected areas with compositions previously characterized by EDS.

Raman spectra were obtained at room temperature (RT) with a Bruker RFS-100 FT–Raman spectrometer provided with a diode-pumped germanium solid-state detector, which operates at liquid nitrogen temperature. A NdYAG laser was used as excitation source with a power ranging from 100 to 400 mW. Powdered samples were pressed in a holder and analyzed (100 scans, 4-$cm^{-1}$ resolution) without further treatment.

FTIR experiments were performed at RT in diffuse reflectance made with a Perkin-Elmer 1750 Fourier transform spectrometer, with a resolution of 4 $cm^{-1}$ accumulating 100 scans. Sample portions were treated for 1 h in pure nitrogen prior to spectrum recording.

Electron paramagnetic resonance (EPR) spectra were recorded at 77 K with a Bruker ER 200 D spectrometer operating in the X-band and calibrated with a DPPH standard ($g = 2.0036$). Portions of ca. 40 mg were placed inside a quartz probe cell with greaseless stopcocks. A conventional dynamic high-vacuum line was used for vacuum or adsorption treatments. The samples were in all cases precalcined under 300 Torr of $O_2$ at 773 K for 2 h. Following this treatment, the samples were outgassed at either 473 or 773 K prior to oxygen adsorption. Oxygen adsorption was performed by admission of a dose of 70 $\mu$mol $g^{-1}$ at 77 K, followed by 30-min warming to RT and 30-min outgassing at 77 K (residual pressure $1 \times 10^{-4}$ mbar).

Isotopic exchange experiments were carried out with ca. 25 mg of sample held inside a recirculating quartz reactor coupled to a grease-free standard vacuum system. Gas phase was analyzed with an online quadrupole spectrometer (Balzers QMG 421 C) connected to the reactor through a metering leak valve. Calcined samples (200 Torr of $^{16}O_2$ at 773 K, 1 h) were subjected to evacuation at reaction temperature (573 K, 10 min) and to a subsequent circulation of ca. 100 Torr of $C^{18}O_2$ at 573 K through the catalytic bed, with continuous analysis of gaseous products ($C^{18}O_2$, $m/Z = 48$; $C^{18}O^{16}O$, $m/Z = 46$; $C^{16}O_2$, $m/Z = 44$; and secondary masses).

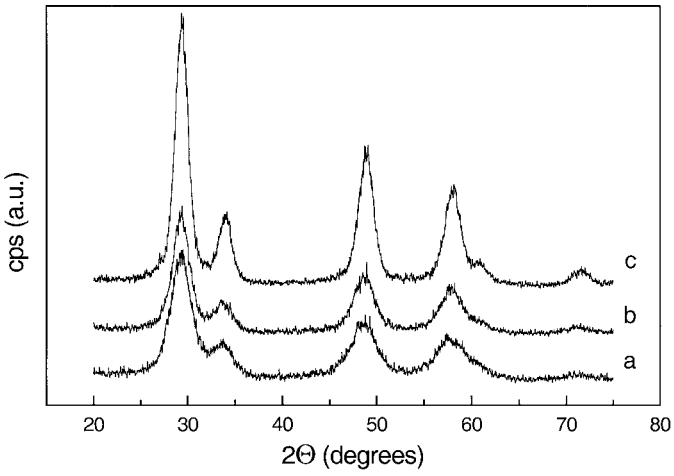


**FIG. 1.** XRD diffractograms of the CZCa and CZ materials: (a) CZCa111, (b) CZCa992, and (c) CZ11.

## RESULTS AND DISCUSSION

### *Structure and Morphology of the Samples*

Powder X-ray diffraction patterns of the CZCa samples, together with the CZ11 reference specimen, are depicted in Fig. 1. This figure gives evidence of the existence of nanosize diffracting entities giving rise to a fluorite-type pattern for both samples (Table 2, Fig. 1). Thus, in all cases the XRD/ED features can be indexed in the Fm3m space group and indicate for the CZCa992 specimen a (pseudo)-cell parameter of $5.28 \pm 0.03$ Å, while for the CZCa111 material the latter parameter takes a value of $5.28 \pm 0.04$ Å. In ceria–zirconia materials, diffraction patterns are dominated by the cation sublattice. Attempts to obtain information concerning cell symmetry were done using the procedure of Yashima *et al.* (5), specifically developed to analyze the tetragonal distortion of the cubic ceria symmetry. Fitting of the (311) (ca. 58°) and, in some cases, (400) (ca. 72°) cubic reflections shows an axial ratio ($c/a$) of 1 within a resolution better than 0.017 (estimated from the full width at half maximum of the (311) reflection). This limited resolution does not allow discerning between Ce–Zr cubic and tetragonal phases and clearly originated from the nanosize nature of the samples. Fortunately (see below), Raman is strongly sensitive to cell structure in covalent oxides and is systematically used in the Ce–Zr system to obtain such types of details (3). According to dark-field TEM pictures (see Fig. 2 and Table 2), particle size seems roughly invariant in the CZCa series, showing an average value close to 2 nm. However, a visible decrease in particle size is detected for the ternary oxides with respect to the corresponding of the CZ11 and some CCa (CCa91) binary mixed solutions (8, 12). The dark-field TEM image (see Fig. 2) also illustrates the precise control of the particle size distribution obtained upon employment of the microemulsion preparation method.

An estimation of the Zr : Ce atomic ratio in the mixed oxide can in principle be made by considering the linear relationship existing for Ce–Zr mixed oxides between the cell parameter and the mentioned atomic ratio (3, 7, 8, 12). The existence of such linear correlation in ternary Ce–Zr–Ca oxides with a constant percentage of Ca of ca. 10 at% has been also shown (10). The comparison of results concerning this Ce–Zr–Ca (containing ca. 10 at% of Ca) vs Ce–Zr mixed oxides indicates that, at least for Zr : Ce atomic ratios below 1 and this level of Ca content, the presence of Ca does not largely affect the value of the cell parameter. Thus, the cell parameter directly measures the Zr : Ce atomic ratio. On the other hand, it must be considered that, as pointed out recently (3), in high-surface Ce–Zr materials, employed as catalyst supports, the slope of this linear correlation is different from that reported for low-surface ceramic oxides, which limits the accuracy of the Zr : Ce atomic ratio estimations made using this method. Nevertheless, assuming the correlations employed for high-surface materials (3), which fits well our data for the set of bulk Ce–Zr binary mixed oxides prepared by microemulsion (results not shown), we can deduce that the XRD-detected fluorite-type entities of both ternary oxides have a Zr : Ce atomic ratio close to 1.

Therefore considering the XRD results just mentioned in addition to the EDS analysis included in Table 2, it can be concluded that the CZCa992 material maintains a relatively high homogeneity in terms of chemical composition,

**TABLE 2**

**XRD/TEM/ED/EDS Main Results**

| Sample | Cell parameter (Å)[a] | Particle size (nm)[b] | $(Zr/Ce)_{at.}$[c] | $(Ca/Ce)_{at.}$[c] | $(Ca/Zr)_{at.}$[c] |
|---|---|---|---|---|---|
| CZCa992 | 5.28[d] | 2 | 0.8–0.95 | 0.15–0.35 | 0.2–0.3 |
| CZCa111 | 5.28[d] | 2 | 0.8–0.9/0.45–0.6 | 0.5–0.8/≈0.9 | 0.6–1.0/1.4–1.7 |

*Note.* See text for details.

[a] Fluorite-type cell with Fm3m symmetry is considered.

[b] From dark-field TEM images taken using the (111) and (200) ED rings of fluorite-type structures.

[c] EDS results. Note that two differentiated zones are detected for CZCa111.

[d] XRD and ED results.

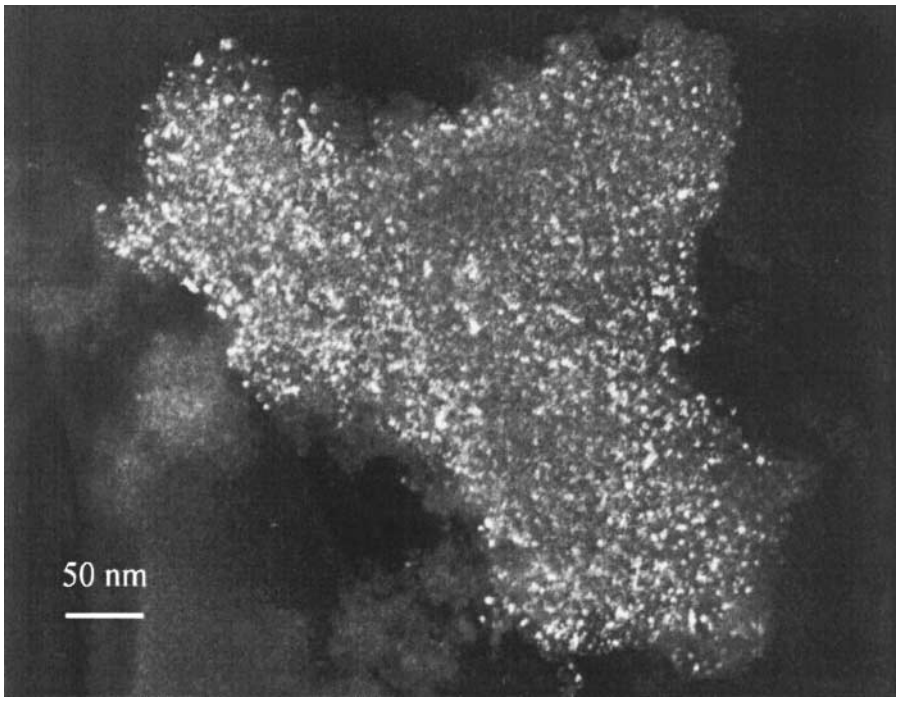


**FIG. 2.** Dark-field TEM image (using the (111) and (200) diffraction rings of fluorite-type lattice) of the CZCa992 specimen.

displaying atomic ratios very close to the nominal ones, e.g., a 1 : 1 Zr : Ce atomic relationship and a Ca content close to 10 at%. These average atomic concentrations can be conveniently represented in a ternary diagram, as shown in Fig. 3, which displays the atomic percentage corresponding to each one of the cations present in the material.

In contrast with the high chemical homogeneity at a molecular scale observed for the CZCa992 material, the CZCa111 specimen is significantly heterogeneous. According to the EDS data (shown in Fig. 3) two types of zones correspond, respectively, to moderate depletions in Ca and Zr with respect to nominal values. Ce seems homogeneously distributed (at the scale detected by EDS), without significant variations between the two zones mentioned, although the EDS values detected are slightly over the nominal one. However, no ED pattern with a Zr : Ce atomic ratio differing from 1 has been detected for a Zr-depleted zone, indicating the exclusive presence of ternary oxide diffracting entities with a Zr : Ce ratio close to 1. This crystalline phase, present in lesser or greater concentration throughout all the CZCa111 material, would be predominant in the zones corresponding to EDS analyses encircled in Fig. 3. The joint consideration of the complete set of results discussed (XRD/ED/EDS) suggests that the crystalline phase can be then viewed as a CZ11 matrix with a limited solubility of cationic Ca. This limit is obviously below the nominal composition of 33 at% and may be compared with the corresponding solubility limit of ca. 30–40 at% detected in the binary CCa mixed oxides prepared by microemulsion (8) or a lower limit (ca. 15 at%) detected in ceramic systems prepared by using a hydrothermal method (13). Therefore, it appears that a rigorous control of local chemical homogeneity as well as particle size must be achieved during preparation of the samples in order to facilitate the substitutional presence of Ca in Ce (or Ce–Zr) cation sublattice positions. Figure 3 roughly indicates that the depletion of Ca with respect to the nominal value (33 at%) would be moderate in our case, as this zone displays an average content of Ca close to 25 at%.

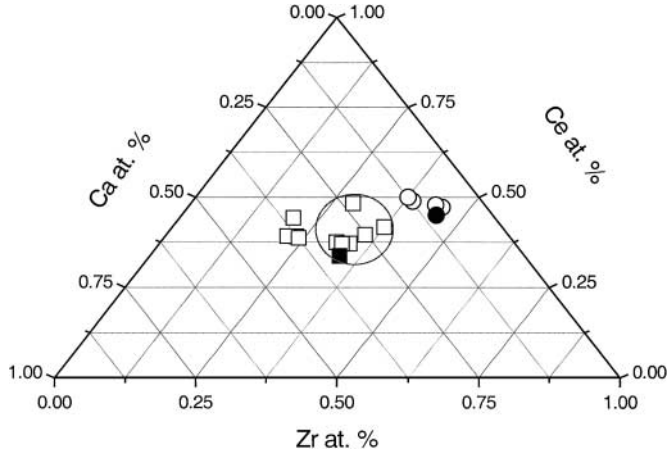


**FIG. 3.** Ternary diagram for EDS atomic percent concentration for the three cationic elements (Ce, Zr, Ca) present in CZCa materials: squares, CZCa111; circles, CZCa992. Closed symbols correspond to average cation concentrations (measured by ICP–AES).

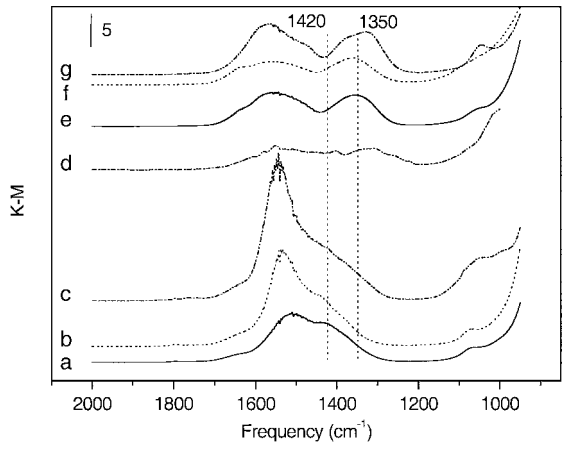


**FIG. 4.** FT-IR spectra of CZCa and reference materials: (a) CZCa111, (b) ZCa11, (c) CCa11, (d) CZ11, (e) CZCa992, (f) ZCa91, and (g) CCa91.

The results just outlined may then suggest that some Ca-richer entites escape detection by diffraction techniques in the CZCa111 specimen. According to EDS, this zone type is characterized (with respect to overall composition values) by a moderate depletion on Zr, a parallel increment in Ca, and deviations of the Zr : Ce atomic ratio well below 1 (see Table 2, Fig. 3). However, as mentioned, even these zones display either ED diffraction characteristics of a crystalline phase with a Zr : Ce atomic ratio close to 1 or, most frequently, absence of diffraction pattern. On the other hand, the IR data shown in Fig. 4 point out to the presence of $Ca^{2+}$ carbonates (even after 773 K calcination), which may likely form part of the diffraction-silent Ca-containing species. Infrared spectroscopy reveals that CZCa (and also CCa and ZCa references) materials contain unidentate (bands at ca. 1500, 1420, and 1060 $cm^{-1}$) and bidentate (bands at ca. 1550, 1315, and 1050 $cm^{-1}$) carbonate species (14, 15). The amount of the former grows at the expense of the latter with the Ca content in the case of ternary materials. Notice that bands at about 2510 and 1795 $cm^{-1}$, typical of bulk calcite, which are present in a Ca reference prepared by microemulsion (calcite appears together with some minor contribution of Ca oxide in this reference material) (8), are not observed in any of the ternary/binary mixed oxides analyzed. In the CCa91 and CZ11 reference specimens, the presence of cerium-related carbonates (band at ca. 1300 $cm^{-1}$) is additionally detected. Estimates based on a TG/MS experiment (thermogravimetry/mass spectrometry) indicate that Ca-containing carbonates, which evolve with maximum at 973 K, yielding exclusively $CO_2$ under dry air up to 1200 K, are about 11.5 wt% (if expressed as $CaCO_3$) of the dehydrated, initial sample, confirming then the relatively low weight of this contribution. Nevertheless, this corresponds to ca. 40 at% of the Ca present in the sample. This datum can be compared with the larger one corresponding to the CCa11 reference (25.6 wt% expressed as $CaCO_3$; 55 at% Ca). Note that these figures are however of a semiquantitative nature, as the EDS atomic ratios reported in Table 2 suggest that the carbonate phase mainly contains Ca but also Ce as cations. The exact location (surface vs bulk) of these $Ca^{2+}$-containing carbonate phases will be analyzed in the next section.

The diffraction (XRD/ED) and TEM/EDS study thus indicates the heterogeneity of the CZCa111 sample, which has two types of zones. One is mainly described as composed by a crystalline Ce–Zr–Ca ternary oxide with a (37.5–37.5–25) average atomic composition while the second has a minor contribution from this phase and is dominated by a Ce–Ca mixed carbonate. The TG/MS study shows that the oxide phase appears to be predominant in the whole system, accounting for about 90% of the material weight.

In contrast to the XRD/TEM results, which yield information related mainly to the cation sublattice, Raman spectra of these fluorite-type oxide structures are dominated by oxygen lattice vibrations (16), which are sensitive to the crystalline symmetry, being thus a potential tool to obtain additional structural information. While $CeO_2$ has only one Raman-active band (due to a vibration mode of $F_{2g}$ symmetry) centered at 465 $cm^{-1}$, in fluorite-type oxides whose crystal symmetry has decreased to the tetragonal $P4_2/nmc$ space group (as in the tetragonal $ZrO_2$ or Ce–Zr mixed oxides with the so called t′ phase), six Raman-active modes are allowed with, respectively, (1) $A_{1g}$, (3) $E_{2g}$, and (2) $B_{1g}$ symmetry (3, 5). In the case of Ce–Zr mixed oxides, the presence of, at most, four bands, two of them clearly visible at 316 and 636 $cm^{-1}$, has been claimed to respond to such symmetry but in a pseudocubic phase called t″ (defined as one which, although belonging to the tetragonal $P4_2/nmc$ space group, has null tetragonality in the cell parameters, i.e., $c/a = 1$) (5). Following this assignment, it can be concluded that our ternary mixed oxides also contain crystalline phases with a pseudocubic t″ structure, displaying the characteristic Raman spectrum (Fig. 5). They therefore maintain the crystalline structure considered most

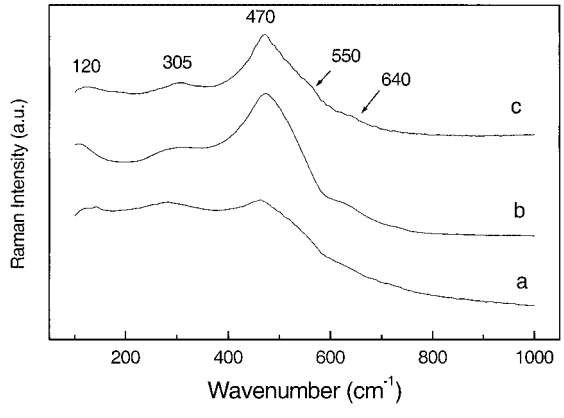


**FIG. 5.** Raman spectra of (a) CZCa111, (b) CZCa992, and (c) CZ11 samples.

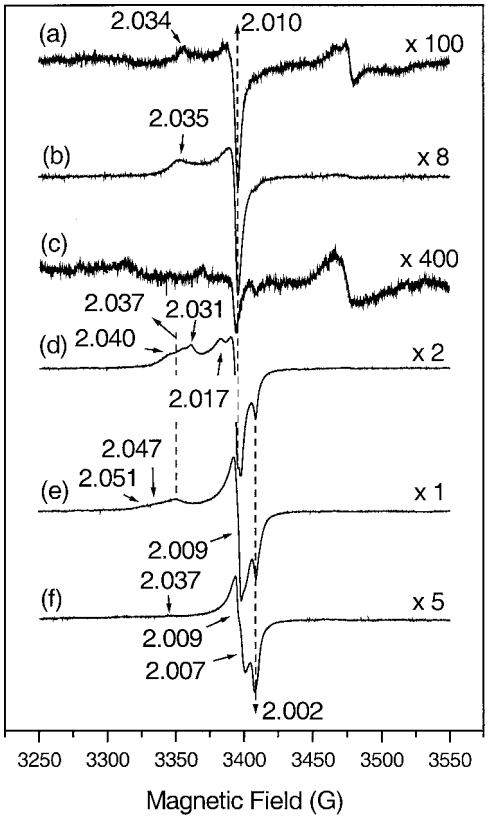


**FIG. 6.** EPR spectra at 77 K following oxygen adsorption at RT (and elimination of excess $O_2$ by pumping at 77 K) on the samples outgassed at $T_v = 473$ or 773 K. (a) CZ11; $T_v = 473$ K. (b) CZCa992; $T_v = 473$ K. (c) CZCa111; $T_v = 473$ K. (d) CZ11; $T_v = 773$ K. (e) CZCa992; $T_v = 773$ K. (f) CZCa111; $T_v = 773$ K.

adequate to obtain optimum oxygen-handling properties (3). The CZCa111 specimen displays less intense and broader Raman modes indicative of the "high" disorder on the anion sublattice of the crystalline ternary oxide phase.

*Oxygen Handling and Surface Properties*

EPR spectra following oxygen adsorption at RT on the CZCa992 and CZCa111 samples, as well as on the CZ11 reference, are shown in Fig. 6. A summary of the characteristics and assignment of the oxygen-related signals detected in these experiments is given in Table 3. All the signals appearing upon oxygen adsorption are attributed to superoxide species chemisorbed at the surface of the samples, their spectral properties being mainly related to the characteristics of the surface (or near surface) cation where the superoxide species are bonded (17). Further details on these attributions can be found elsewhere (8, 17–20).

The spectra observed upon oxygen adsorption on the samples outgassed at 473 K (Figs. 6a–6c) are essentially constituted of $Ce^{4+}$–$O_2^-$ species (Table 3), indicating that surface vacancies are created almost exclusively at the environment of Ce cations upon that treatment. A significantly higher intensity of these $Ce^{4+}$–$O_2^-$ radicals is detected for the CZCa992 sample with respect to the CZ11 reference. This indicates that the presence of calcium facilitates generation of surface oxygen vacancies coordinated to cerium cations and/or modifies the electronic characteristics of the material to enhance electron transfer toward oxygen (20, 21). Modification of the electronic characteristics of the Ce-based material, particularly favoring the reduction of Ce(IV) to Ce(III), has been already observed and theoretically analyzed in CCa binary oxides (21). The intensity decrease observed for the CZCa111 sample (Fig. 6c) must thus be primarily attributed to a calcium enrichment at the surface of the sample, as previously proposed to occur for the CCa11 sample (8). This is supported by the fact that the spectrum observed for this sample after oxygen adsorption on the sample outgassed at 773 K is constituted almost exclusively of $Ca^{2+}$–$O_2^-$ species (no significant feature attributable to the presence of either Ce or Zr entities is visible in Fig. 6f below a $g$ value of 2.006). It must be noted that considering the low reducibility of the corresponding cations, formation of $Ca^{2+}$–$O_2^-$ and $Zr^{4+}$–$O_2^-$ would probably follow a spillover-like process whereby oxygen is first activated (with formation of the superoxide species) at reduced cerium sites (formally cus $Ce^{3+}$ species), while in a posterior step the $O_2^-$ species formed is transferred to the corresponding $Ca^{2+}$ or $Zr^{4+}$ adsorption site (8, 18, 22).

The spectra observed for CZ11 and CZCa992 following oxygen adsorption on the samples outgassed at 773 K are complex and constituted of the overlapping of different superoxide species (Figs. 6d and 6e). In this case, the outgassing treatment is believed to allow, at least qualitatively,

**TABLE 3**

**Characteristics of the EPR Signals Obtained upon Oxygen Adsorption on the Outgassed CZCa Samples**

| EPR parameters[a] | Assignment | Reference |
|---|---|---|
| $g_\parallel = 2.035$–$2.034$, $g_\perp = 2.010$ | $Ce^{4+}$–$O_2$ formed at isolated oxygen vacancies | 19 |
| $g_z = 2.051$–$2.040$, $g_y = 2.010$–$2.009$, $g_x = 2.009$–$2.008$ | $Ce^{4+}$–$O_2^-$ formed at associated oxygen vacancies | 19 |
| $g_z = 2.037$, $g_y = 2.009$, $g_x = 2.002$ | $Zr^{4+}$–$O_2^-$ | 18 |
| $g_y = 2.007$, $g_x = 2.002$ | $Ca^{2+}$–$O_2^-$ | 17 |

[a] No reasonably narrow feature was detected for $g_z$ of $Ca^{2+}$–$O_2^-$ species upon magnetic field sweeping from $g \approx 2.3$. This coincides with results observed for the CCa series and can be attributed to a large heterogeneity of $Ca^{2+}$ adsorption sites (8).

the analysis of the whole cationic surface distribution due to the existence of vacancies around all cations, irrespective of their chemical nature, and the mentioned spillover process (8, 17–19, 22). Both ternary oxides show $Ce^{4+}$–$O_2^-$ species and $Zr^{4+}$–$O_2^-$ species while the presence of scarce amounts of $Ca^{2+}$–$O_2^-$ species in the CZCa992 specimen is suggested by the presence of a shoulder at $g \approx 2.007$. As mentioned, the $Ca^{2+}$–$O_2^-$ contribution dominates the CZCa111 spectra with small contributions of the remaining superoxide species. On the other hand, the higher overall intensity of superoxide radicals detected for CZCa992 with respect to the CZ11 sample in the experiments performed over the samples outgassed at 773 K and the larger $g_z$ values observed for the $Ce^{4+}$–$O_2^-$ radicals (19) in the former (Figs. 6d and 6e) suggest again that calcium presence facilitates generation of surface oxygen vacancies at the coordinative environment of both cerium and zirconium cations.

The effect of Ca on the surface reducibility may then be primarily correlated with the depletion of Ce from the surface layer, but also with a combined effect of its electronic influence on the material properties (facilitating Ce reduction, in agreement with previous work (21)) and the different chemical coordination of this (Ca) ion at the surface of our two ternary specimens. The similarity of IR spectra eliminates any difference attributable to the Ce-alone carbonates when comparing the CZCa992 and CZ11 samples, showing that the CZCa992 specimen contains bidentate carbonates while the CZCa111 one is dominated by unidentate species. The presence of Ca mainly at the surface (EPR) and the absence of any well-developed, crystalline carbonate phase (XRD, IR) strongly indicates the surface location of such carbonate species; therefore, the larger stability of the unidentate carbonate (14) may further contribute to the lower surface reducibility displayed by materials with high Ca content (possibly by modifying the oxygen molecule interaction with the surface). In any case, it appears clear that during formation of ternary mixed oxides Ca tends to be the last cation to precipitate, probably producing a positive gradient of Ca concentration in going from the bulk to the surface, yielding a material with a Ca-enriched surface and near-surface regions. Ca is then proposed to induce geometric effects, depleting Ce surface content with respect to the CZ11 reference, as well as electronic ones, favoring surface Ce (and maybe Zr) reduction. Other consequences of Ca surface segregation and associated formation of Ca-related carbonates for the samples with relatively high Ca loadings are related to the apparent surface area decreases observed for the binary CCa11 and ZCa11 samples and the stronger effect of this kind (the origin of which remains unclear) observed for the CZCa111 ternary system (Table 1).

The strongly different behavior detected between the CZCa samples in surface oxygen handling properties is again encountered when analyzing the oxygen bulk mobility. Oxygen isotopic exchange experiments using labeled $C^{18}O_2$ were carried out on these samples; after the work by Duprez and colleagues these data can be conveniently used to obtain a measure of the bulk diffusion coefficient (23, 24). Bulk oxygen coefficient ($D_b$) is calculated according to the Kakiota model (25),

$$\mathrm{Ln}\left(F^{18}O_g - F^{18}O_s\right) = -C_1 D_b^{1/2} t^{1/2} + C_2, \qquad [1]$$

where $F^{18}O$ corresponds to $^{18}O$ fractional percentage in the gas phase ($g$) and initial in the solid ($s$), $t$ is time, and $C_x$ are constants. Obviously, when $C^{18}O_2$ is contacted with the solid, surface exchange via adsorption–desorption of carbonate species must occur; this corresponds to the first part of the curves displayed in Fig. 7. Further exchange of oxygen (after surface equilibration) can only proceed at the bulk of the specimen and, according to Equation [1], would obey a linear relationship between its logarithmic form and the square root of time. It must be noted that this equation only applies if surface equilibration is quicker than bulk exchange, as has been shown in many oxides, including ceria, if a correct experimental method is used (23, 25, 26). It can be also noted that for obtaining this kind of information with experiments employing $^{18}O_2$, it is necessary to preactivate the molecule (dissociation) over small quantities of noble metals at the surface of the oxide (23), a requirement not necessary with the more labile bond of $C^{18}O_2$ (25, 26), but that, on the other hand, can yield additional information on surface diffusion coefficients. Although the value of the oxygen bulk oxygen diffusion coefficient extracted by this method may be subject to discussion, the trend detected in the set of samples is a clear indication of the ease

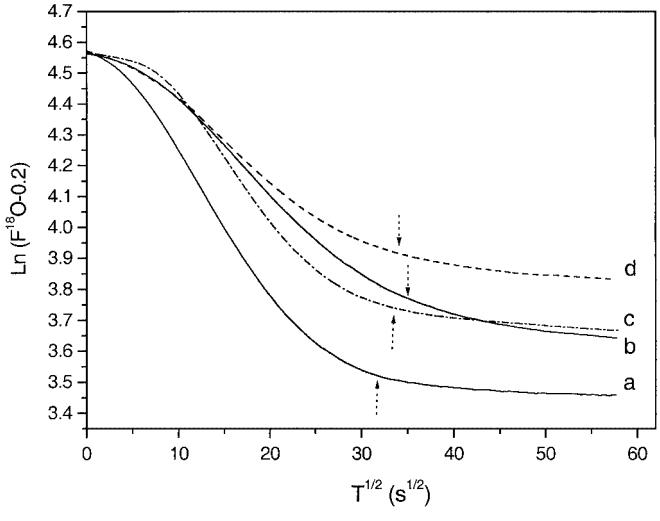


**FIG. 7.** Logarithm of $^{18}O$ fractional percentage at the gas phase vs square root of time. (a) CZCa992, (b) CZCa111, (c) CCa11, and (d) CZ11. Arrows indicate the (approximate) starting point for bulk exchange. See text for details.

**TABLE 4**

**Coefficients for Oxygen Bulk Diffusion at 573 K**

| Sample | $D_b$ ($10^{-21}$ cm$^2$ s$^{-1}$) |
|---|---|
| CZ11 | 84 |
| CCa11 | 18 |
| CZCa992 | 35 |
| CZCa111 | 577 |

*Note.* See text for details.

in the management of oxygen by the bulk of the material (8, 23–26).

Results using this analysis are shown in Table 4. From this table it can be concluded that the addition of Ca in moderate amounts somewhat reduces the oxygen mobility at the bulk while higher loadings strongly enhance this property with respect to the CZ11 reference. The value obtained for the CZCa992 material is however similar to that of the $CeO_2$ reference prepared by microemulsion (8). The presence of two types of phases (ternary oxide and Ce–Ca carbonate) may complicate the analysis of the CZCa111 result; however by combining the TG/MS and EDS measurements it can be calculated that oxygen is approximately distributed in a 3.6 : 1 ternary oxide : carbonate atomic ratio, suggesting that this result may be mainly associated with the oxidic phase. Moreover, comparison with results obtained for the CCa11 sample (see Table 1), which also contains the carbonate phase (8), confirms this point. Measurements of bulk ionic conductivity ceramic on Ce : Zr : Ca ternary solutions (rich in zirconium) at high temperatures (above 973 K) show a proportionality with the number of intrinsic anionic vacancies up to above a 12 at% content of Ca, decreasing at about this cutoff level (27). In principle, this relationship is linear for a low-vacancy concentration and appears to be general for Ce-containing oxidic materials (28). The existence of such a limiting level above which ionic diffusion decreases has been attributed to ordering/association of vacancies. No clear explanation can be put forward to interpret the different behavior displayed by our samples, with the marked growth of oxygen bulk diffusion for the CZCa111 sample, although the presence of Ca seems to reduce, at least at the surface, the number of associated vacancies in nanosize CCa (8) as well as in Ce–Zr–Ca ternary nanosize systems (this work), and this may also happen in the bulk. Due to the gradient in Ca concentration expected in the ternary oxide particles, it is not clear whether the bulk content of these specimens is below 12 at%; however no classical behavior, e.g., linear correlation, is detected in this study between nonstoichiometry and bulk oxygen conductivity. The trend detected is, in any case, similar to that reported for binary CCa samples, indicating that the Ca effect may be independent of the particular anion sublattice symmetry (8), although it is clearly stressed when going from cubic (ceria) to tetragonal (Ce–Zr) symmetries. Whether the physical basis of the different behavior can be attributed to the larger Ce content (with respect to ceramic samples) of our ternary oxides and/or whether it is an intrinsic property of vacancy association energy behavior of nanosize materials remains to be verified.

In brief, the presence of Ca induces important modifications on the oxygen handling properties of Ce–Zr mixed oxide materials. These alterations are strongly dependent on Ca content and may markedly influence the behavior of Ce-containing components. Considering oxygen transport properties, because they are frequently limited by the bulk step (as detailed above), it can be said that Ca and Zr can produce additive, enhancing effects and may have a clear application in Ce-based membranes. Concerning catalytic aspects, the modification of surface vacant distribution has an impact on the interaction of the solid with oxidants, like those present in exhaust streams of automobiles. With respect to reactivity toward NO, the Ca-induced modifications of the distribution of isolated and associated vacancies at the surface of the samples can have consequences on its preferential dissociative activation (leading to $N_2/N_2O$ formation), with the consequent impact on the activity/selectivity of the materials for NO reduction reactions (29). The properties of Ce-containing materials on oxygen storage capacity (OSC) or oxygen storage complete capacity (OSCC) have been recently reviewed (3, 30). Zr addition to ceria improves both properties. Differences between OSC and OSCC in Ce–Zr materials appears to be related with the presence of "very reactive" sites, which are those mainly involved in storage in dynamic conditions (OSC) and are then of significant importance in TWC systems working in real conditions. Ca can play an important role in favorably altering such sites, as our experiments show the very easy formation of surface vacancies at low concentration as well as a significant enhancement of bulk oxygen diffusion at high concentration, but always at low temperatures ($T < 573$ K). Further experiments are now under way to study this latter point.

## CONCLUDING REMARKS

To summarize the geometrical/morphological characteristics of the CZCa ternary mized oxides prepared by microemulsion, we can say that addition of Ca to a ceria–zirconia material (while keeping a Zr : Ce atomic ratio of 1) produces a crystalline oxidic phase which maintains the pseudocubic t″ structure and unit cell parameters of the initial CZ11 binary oxide but clearly decreases the average particle size (measured by TEM) to a value close to 2 nm, irrespective of the Ca content of the specimen. This decrease in size is likely due to the presence of anion vacancies. High homogeneity of the crystalline phase in terms of chemical

composition is observed, although it may decrease with the percentage of Ca present. A Ca solubility limit of about a 25 Ca at% is detected in the ternary mixed oxide, somewhat paralleling the behavior of the CCa binary series (8). In the CZCa111 specimen, a diffraction-silent phase is also present as a minor contribution. Excess calcium (e.g., the part which is not soluble in the crystalline phase) appears to be mainly present in the form of mixed Ce–Ca carbonates, which tends to be at the surface of the sample.

The mentioned structural/morphological characteristics of the CZCa materials allow us to qualitatively interpret their oxygen handling properties. Insertion of Ca in a CZ11 binary system appears to influence strongly the interaction with oxygen molecules. Oxygen activation at the surface (via superoxide formation) appears strongly enhanced when moderate amounts of Ca are present but is strongly inhibited when Ca dominates this layer. The depletion of surface Ce centers and their electronic modification are proposed to be on the origin of this behavior. Contrarily, oxygen bulk diffusion appears mildly hindered/strongly enhanced at low/high Ca atomic content materials. The latter property parallels the (weaker) behavior detected in CCa fluorite-type binary oxides and would appear insensitive to the concentration of intrinsic anionic vacancies located at the bulk of such nanosize materials.

## ACKNOWLEDGMENTS

Thanks are given to Dr. E. Sastre, Mr. F. Sanchez, and Mrs. L. N. Salamanca for performing the TG/MS, EPR, and TEM experiments, respectively and to Dr. J. A. Anderson for the use of the infrared spectrometer. Support from CICYT (Project MAT 2000-1467) is fully appreciated.

## REFERENCES

1. Che, M., and Bennet, C. O., *Adv. Catal.* **36**, 55 (1989).
2. Kofsta, P., "Non-Stoichiometry, Diffusion and Electrical Conductivity of Binary Mixed Oxides." Wiley, New York, 1972.
3. Kaspar, J., Fornasiero, P., and Graziani, M., *Catal. Today* **50**, 285 (1999).
4. Nigara, Y., Watanabe, W., Mizusaki, J., and Ishigame, M., *J. Electrochem. Soc.* **144**, 1050 (1997).
5. Yashima, M., Arashi, H., Kakihana, M., and Yoshimura, M., *J. Am. Ceram. Soc.* **77**, 1067 (1994).
6. Vlaic, G., Fornasiero, P., Geremia, S., Kaspar, J., and Graziani, M., *J. Catal.* **168**, 386 (1997).
7. Zhang, Y., Anderson, S., and Muhammed, M., *Appl. Catal. B* **6** (1995) 325.
8. Iglesias-Juez, A., Hungría, A. B., Gálvez, O., Martínez-Arias, A., Fernández-García, M., Guerrero-Ruiz, A., Conesa, J. C., and Soria, J., *Stud. Surf. Sci. Catal.* **138**, 347 (2001).
9. Terribile, D., Trovarelli, A., de Leitenburg, C., Primavera, A., and Dolcetti, G., *Catal. Today* **47**, 133 (1999).
10. Nigara, Y., Watanabe, K., Kawamura, K., Mizusaki, J., and Kawada, T., *J. Am. Ceram. Soc.* **144**, 1050 (1997).
11. Zhang, Q., Lu, W. X., He, F., Chen, Y. R., and Wu, H. Z., *J. Mater. Sci. Lett.* **19**, 1093 (2000).
12. Martínez-Arias, A., Fernández-García, M., Ballesteros, V., Salamanca, L. N., Otero, C., Conesa, J. C., and Soria, J., *Langmuir* **15**, 4796 (1999).
13. Huang, W., Shuck, P., and Greenblatt, M., *Chem. Matter.* **9**, 2240 (1997).
14. Fukuda, Y., and Tanabe, K., *Bull. Chem. Soc. Jpn.* **46**, 1616 (1973).
15. Mikkelsen, A., Engelsen, S. B., Hansen, H. C. B., Larsen, O., and Skibsted, L. H., *J. Cryst. Growth* **177**, 125 (1997).
16. Ferraro, J. R., and Nakamoto, K., "Introductory Raman Spectroscopy." Academic Press, New York, 1994.
17. Che, M., and Tench, A. J., *Adv. Catal.* **32**, 1 (1983), and references therein.
18. Martínez-Arias, A., Fernández-García, M., Belver, C., and Conesa, J. C., *Catal. Lett.* **65**, 197 (2000).
19. Soria, J., Martínez-Arias, A., and Conesa, J. C., *J. Chem. Soc. Faraday Trans.* **91**, 1669 (1995).
20. Anpo, M., Che, M., Fubini, B., Garrone, E., Giamello, E., and Paganini, M. C., *Top. Catal.* **8**, 189 (1999).
21. Carolis, S., Pascual, J. L., Pettersson, L. G. M., Baudin, M., Wojcik, M., Hermansson, K., Palmqvist, A. E., and Muhammed, M., *J. Phys. Chem. B* **103**, 7627 (1999).
22. Martínez-Arias, A., Fernández-García, M., Hungría, A. B., Conesa, J. C., and Munuera, G., manuscript in preparation.
23. Martin, D., and Duprez, D., *J. Phys. Chem. B* **100**, 9429 (1996).
24. Martin, D., and Duprez, D., *J. Phys. Chem. B* **103**, 7627 (1999).
25. Kakiota, H., Ducarme, V., and Teichnier, J., *J. Chim. Phys.* **68**, 1715 (1971).
26. Guerrero-Ruiz, A., Rodríguez-Ramos, I., Ferreira-Aparicio, P., and Volta, J. C., *Catal. Lett.* **45**, 113 (1997).
27. Kawamura, K.-I., Watanabe, W., Nigara, Y., Kaimai, A., Kawada, T., and Mizusaki, J., *J. Electrochem. Soc.* **145**, 2552 (1998).
28. Trovarelli, A., *in* "Catalysis by Ceria and Related Materials" (A. Trovarelli, Ed.), Ch. 2. World Scientific, London, 2002.
29. Martínez-Arias, A., Soria, J., Conesa, J. C., Seoane, X. L., Arcoya, A., and Cataluña, R., *J. Chem. Soc. Faraday Trans.* **91**, 1679 (1995).
30. Duprez, D., and Descorme, C., *in* "Catalysis by Ceria and Related Materials" (A. Trovarelli, Ed.), Ch. 7. World Scientific, London, 2002.